

Neural-Network Quantum Embedding Solvers for Correlated Materials

A. Valenti,¹ I. Park,¹ A. Georges,^{1,2,3,4} A.J. Millis,^{1,5} and O. Parcollet^{1,6}

¹Center for Computational Quantum Physics, Flatiron Institute, 162 5th Avenue, New York, NY 10010, USA

²Collège de France, 11 place Marcelin Berthelot, 75005 Paris, France

³CPHT, CNRS, Ecole Polytechnique, IP Paris, F-91128 Palaiseau, France

⁴DQMP, Université de Genève, 24 quai Ernest Ansermet, CH-1211 Genève, Suisse

⁵Department of Physics, Columbia University, 538 West 120th Street, New York, NY 10027, USA

⁶Université Paris-Saclay, CNRS, CEA, Institut de Physique Théorique, 91191, Gif-sur-Yvette, France

(Dated: March 18, 2026)

Quantum impurity solvers are the computational bottleneck of quantum embedding approaches to correlated materials, such as dynamical mean-field theory (DMFT). We show that neural networks trained on synthetic, material-agnostic data learn the impurity mapping from hybridization functions and local interactions to Green’s functions with quantitative accuracy for both model systems and real materials, providing fast solvers for single- and multi-orbital models. Benchmarks against numerically controlled quantum Monte Carlo show that the method reproduces the Mott transition, multi-orbital phase diagrams of Hubbard-Kanamori models, and the electronic properties of SrVO₃ and SrMnO₃. The learned solvers achieve orders-of-magnitude speedup and can initialize controlled calculations, dramatically accelerating DMFT while preserving accuracy.

The *many electron problem* [1], one of the grand challenges of modern science, consists of computing experimentally measurable correlation functions of a system of interacting electrons in a solid, given some basic knowledge of atomic structure and some external parameters such as chemical potential and temperature. Due to the exponential growth of Hilbert space with system size, it is a notoriously hard high-dimensional problem whose solution has motivated decades of development of theoretical and computational methods. Neural networks (NN) offer a promising approach to this challenge as their architectures efficiently approximate high-dimensional functions, capturing complex correlations and exhibiting strong generalization from data.

Quantum embedding methods such as Dynamical Mean Field Theory (DMFT) [2–4] form a well-established theoretical framework for studying the electronic structure of strongly correlated materials and related theoretical models. They reduce the complex many-electron problem to solving an auxiliary ‘quantum impurity’ (QI) model, consisting of a finite number of localized orbitals or sites coupled to a self-consistently determined, non-interacting electronic bath. While QI ‘solvers’ – algorithms [5–14] for solving quantum impurity models – are available, they have a significant computational cost. Reducing this cost could transform the field by speeding up computations of strongly correlated materials with DMFT combined with density functional theory (DFT+DMFT) [4, 15, 16] to the level of DFT computations routinely used for weakly correlated ones.

A quantum impurity solver is a high dimensional function, returning the impurity Green’s functions from the parametrization of the bath and the values of the atomic interactions. In this letter, we show that neural networks trained on simulated ground-truth data provide a powerful, flexible and general representation of quantum impurity solvers that can be successfully used to compute the electronic structure of materials with strong correlations

within DFT+DMFT. We go beyond previous machine learning approaches to DMFT [17–23], by constructing a set of NN quantum impurity solvers for one-, two-, and three-orbital models using synthetic training data obtained from systematically sampling bath parametrizations and interactions, independently of the electronic structure details of specific materials. We benchmark our NN solvers in various DMFT computations: the first-order Mott transition in the single-band Hubbard model, the phase diagram of a two-orbital Hubbard-Kanamori model, and DFT+DMFT computations of two materials (SrVO₃, a correlated metal, and SrMnO₃, a Mott insulator). In all cases, we find excellent agreement with controlled solvers, demonstrating that NN-based solvers trained on synthetic data perform reliably on a broad domain of applications.

Neural network solvers are extremely fast, requiring seconds even for multiorbital materials compared to hours or days for controlled numerical solvers such as continuous time quantum Monte Carlo (CT-QMC) [5–7] or tensor networks [13, 14], thereby enabling numerous applications. However, a lack of accuracy control is inherent in machine learning methods. We show that controlled accuracy can be obtained by using NN solvers as accelerators, performing a few refinement iterations with an accurate solver starting from a converged solution obtained efficiently with the NN solver.

Setup— A QI problem is entirely specified by: (i) a hamiltonian H_{int} describing local many-body interactions among the M local orbitals defining the embedded atomic shell - with $m = 1, \dots, 2M$ labeling both spin and orbital indices; (ii) a matrix of local levels ϵ_{mm}^d (in which the overall chemical potential μ can be included) and (iii) a set of functions $\Delta_{mm'}(\tau)$ (the dynamical mean-field, or hybridization function) which encode the transfer of electrons between the local atomic shell and the self-consistent bath. Here, τ is the imaginary time which runs from $\tau = 0$ to $\tau = \beta \equiv 1/T$,

the inverse temperature. The precise formulation of the imaginary-time effective action describing the QI model is given in Appendix A, together with the Hubbard and Hubbard-Kanamori forms of the interaction hamiltonian H_{int} considered in this work, parametrized by the screened Coulomb interaction U and Hund’s coupling J . A QI solver is a high-dimensional function:

$$(H_{\text{int}}, \beta, \epsilon_{mm'}^d, \Delta_{mm'}(\tau)) \rightarrow G_{mm'}(\tau) \quad (1)$$

that returns the impurity Green’s function $G_{mm'}(\tau)$ from the local levels $\epsilon_{mm'}^d$, the dynamical mean-fields $\Delta_{mm'}(\tau)$, and the parameters H_{int}, β .

In order to facilitate the network’s task, we use a parsimonious representation of the functions Δ and G on the imaginary axis, as vectors $\{\Delta(\tau_i)\}, \{G(\tau_i)\}$, where $\{\tau_i\}$ with $1 \leq i \leq N_\tau$ is a compact Discrete Lehman Representation (DLR) mesh [24]. This grid uses a minimal number of points $N_\tau \sim \log(\beta\omega_{\text{max}})\log(1/\epsilon)$ which increases logarithmically as a function of β , the high-energy cutoff ω_{max} (the maximum support of the spectral functions) and the precision ϵ . In this work, $N_\tau < 10^2$.

As we want to train our NN solver for a range of temperatures, using a different grid for each β would a priori require the use of NN architectures that can deal with input data of different sizes. We circumvent this challenge by noting that, from the spectral representation, the function $G(\tau)$ can be viewed as a function of τ/β with a high energy cutoff $\beta\omega_{\text{max}}$ (which may depend on interaction). To represent our functions for a range of temperatures $[0, \beta_M]$, we therefore use the *same* DLR grid generated for $\beta = \beta_M$, cutoff ω_{max} and precision ϵ (see Appendix C).

The crucial ingredient in building a neural-network QI solver is the training dataset. Our aim is to construct a well-defined, general-purpose QI solver that is usable in any DMFT computation within its specified range of parameters (e.g. temperatures, interactions)- rather than a solver applicable only to a specific class of materials or band structures. To avoid material-specific bias, we purposefully utilize a *synthetic* dataset, which we create in three steps. First, we randomly draw a set \mathcal{D}_1 of hybridization functions using random coefficients in the DLR representation in terms of a sum of N_τ exponentials [24]. Second, we solve the QI model for all $\Delta_j \in \mathcal{D}_1$ to obtain G_j using a numerically exact continuous time Quantum Monte-Carlo (CTSEG [5, 6] for 1 orbital, or CTHYB for 2 and 3 orbitals). In ML parlance, $(H_{\text{int}}, \beta, \epsilon_{mm'}^d, \Delta_{mm'}(\tau))_j$ constitute the input features, and G_j are the corresponding labels. Third, we augment our dataset by applying 1 – 2 DMFT iterations with a simple self-consistency condition $\Delta = G$, and randomly varying H_{int} (and, if included, β) between iterations. This augmentation is crucial for the quality of the NN solver. Remarkably, we show below that the solver generalizes well and performs effectively for DMFT computation of materials where the self-consistency condition is far more complex.

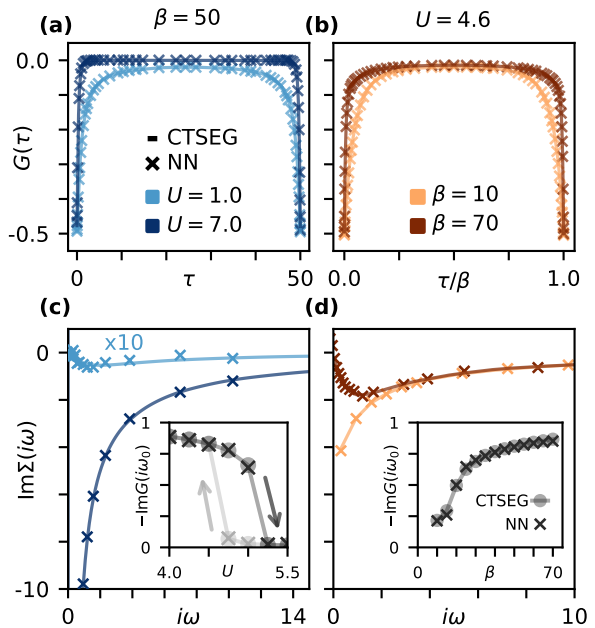


FIG. 1. Comparison of the GNet solver (symbols) with CTSEG (lines) for the half-filled one orbital DMFT solution of the Hubbard model on the Bethe lattice. Left column: U -scan at $\beta = 50$. Right column: β -scan at $U = 4.6$. (a,c) $G(\tau)$ (a) and $\text{Im}\Sigma(i\omega)$ (c) for $U \in \{1, 7\}$. On panel (c), for $U = 1$, $\text{Im}\Sigma(i\omega)$ is multiplied by 10 for readability. (b,d) Same for $\beta = 10, 70$. Inset (c) $-\text{Im}G(i\omega_0)$ vs U showing DMFT metal-insulator transition hysteresis, with grey (black) arrows indicating insulating (metallic) branches. Inset (d) $-\text{Im}G(i\omega_0)$ vs β , close to the Mott transition.

We train a set of feed-forward neural network QI solvers for M orbital systems with $M = 1, 2, 3$. In the following, we refer to them as GNet. The total number of training examples is 1.6×10^4 (resp. $1.8 \times 10^4, 8.6 \times 10^4$) for $M = 1$ (resp. $M = 2, 3$). We also train a solver for the density n for 3-orbital systems, as it yields more precise results than deducing n from GNet. Details of the neural networks, the training set, and the computational cost are presented in Appendix B.

1-orbital model— Fig. 1 compares results obtained from our GNet solver (trained at the range of $\beta \in [10, 80]$) to numerically exact results obtained with a CTSEG quantum Monte-Carlo algorithm [5, 6], for the conceptually simplest case: the DMFT non-magnetic solution of the half-filled one orbital Hubbard model on the Bethe lattice [3] (semi-circular density of states with bandwidth normalized to 4) [25]. Additional results away from half-filling are presented in Appendix D. This model exhibits a paramagnetic metal to paramagnetic insulator (“Mott”) transition as the interaction strength U is increased above a critical value. Panel (a) shows that the NN-computed imaginary time Green’s function is indistinguishable from the numerically exact ground truth data for two very dif-

ferent interaction strengths; one below and one above the critical value for the Mott transition. Panel (b) shows that the NN solver also correctly reproduces the temperature dependence even for an interaction strength close to the Mott critical value [3]. Figure 1(c,d) shows the corresponding self-energies, obtained via the Dyson equation

$$\Sigma_{mm'}(i\omega_n) = i\omega_n\delta_{mm'} - \epsilon_{mm'}^d - \Delta_{mm'}(i\omega_n) - G_{mm'}^{-1}(i\omega_n).$$

In both cases, we observe an excellent agreement between the two solvers. The insets in Fig. 1(c,d) present a more detailed examination of the Fourier transform of G evaluated at the lowest Matsubara frequency, $\omega_0 = \pi T$. G Net correctly reproduces the hysteresis (bistable behavior) occurring in the DMFT approximation to the interaction-driven Mott transition [3] (inset in panel (c)) as well as the temperature dependent change from insulating (low G) behavior at high T (small β) to metallic (high G) at low T (inset in panel (d)).

2-orbital phase diagram— We now show that G Net reliably captures the richer physics of multi-orbital Hubbard-Kanamori models [26, 27]. In the presence of crystal field splitting, the local interaction Hamiltonian becomes

$$H_{\text{int}} = H_{\text{H-K}}(U, J) + \sum_{\sigma} \Delta_{\text{cf}}(n_{1,\sigma} - n_{2,\sigma}), \quad (2)$$

where $H_{\text{H-K}}$ is the Hubbard-Kanamori interaction Hamiltonian (see Appendix A) and $n_{i,\sigma}$ denotes the occupancy of orbital i and spin σ . Two-orbital models arise for example in the context of materials involving transition metals with partially filled d -shells. The key parameters in addition to the density of states are a "charging energy" U , a multiplet-splitting energy J (Hund's coupling) and a crystal field splitting Δ_{cf} . At half-filling, the interplay between these energies leads to a sequence of orbital polarization transitions [28].

Using the G Net solver for $M = 2$ orbitals trained at $\beta = 50$, we determine the DMFT phase diagram of this model on the Bethe lattice (defined as above). The metal-insulator transition is identified by monitoring the value of $-G(\beta/2)$, and the results are compared with the CTHYB results of Ref. [28], as shown in Fig. 2(a). The insets in Fig. 2(b,c) show this criterion, $-G(\beta/2)$, at selected values of U, J as a function of Δ_{cf} . A jump indicates the position of the phase transition. We find that the phase diagram is consistent with that of Ref. [28], within a few percent of critical parameter values. We further compare the Green's functions in panels (b) and (c) between the G Net solver (crosses), fully converged using Δ -mixing ($\Delta_{i+1} = \gamma\Delta_i + (1-\gamma)\Delta_{i-1}$, with i the iteration number of the self-consistent loop), and the CTHYB results (solid lines), finding good agreement.

3-orbital materials— Finally, we demonstrate the application of G Net to DFT+DMFT calculations for real materials and how it accelerates computationally demanding DFT+DMFT calculations. We show two real material examples, SrVO_3 [29], a moderately correlated metal,

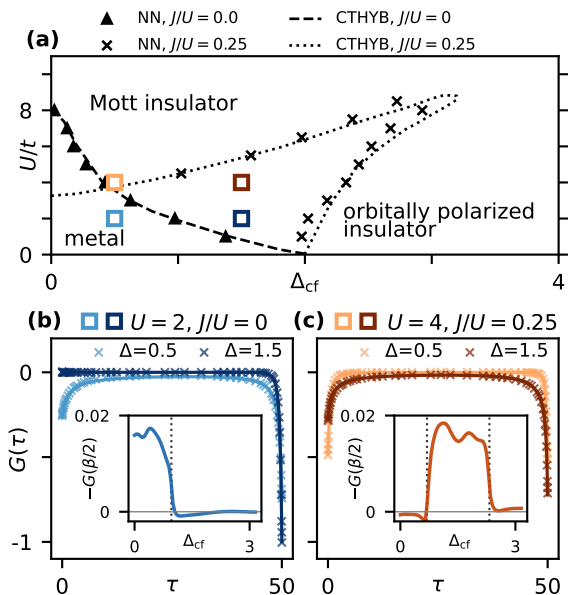


FIG. 2. (a) Metal-insulator phase boundaries obtained using G Net for 2-orbital at $\beta = 50$ (markers), compared with the CTHYB results from Ref. [28]. The colored squares denote the parameter values at which the Green's functions are directly compared with CTHYB in panels (b) and (c). Blue squares denote $J/U = 0$, while orange/red squares denote $J/U = 0.25$. Crosses in panels (b) and (c) denote the NN solutions, whereas solid lines denote the CTHYB results. The insets show the NN-predicted $G(\beta/2)$ along horizontal cuts in the phase diagram. The vertical dotted lines in the insets correspond to the position of the phase transition taken from Ref. [28].

and SrMnO_3 [30, 31], a strongly correlated Mott insulator. The DMFT impurity model for both cases involves three orbitals corresponding to the t_{2g} multiplet of the V or Mn atoms with cubic symmetry. For these calculations, we use the G Net solver for $M = 3$ orbitals at $\beta = 10$ in combination with the NN density-solver (see Appendix E for details.)

Figure 3 compares the G Net solver results (crosses) with a CTHYB reference calculation (solid blue line). The agreement is excellent for the Green's function $G(\tau)$, while the self-energy (obtained via the Dyson equation) exhibits good but slightly lower accuracy. These calculations are performed at a fixed chemical potential μ , which gives the target density determined from DFT calculation. The insets in the upper panels show the impurity occupancy $n(\mu)$ for various chemical potentials, computed with the NN density-solver at the final G Net DMFT iteration. This solver predicts the density more accurately than if directly computed from the G Net result at the final DMFT iteration, and again shows very good agreement with CTHYB. These results show that G Net provides accurate results for DFT+DMFT computations of two materials, despite being trained only on

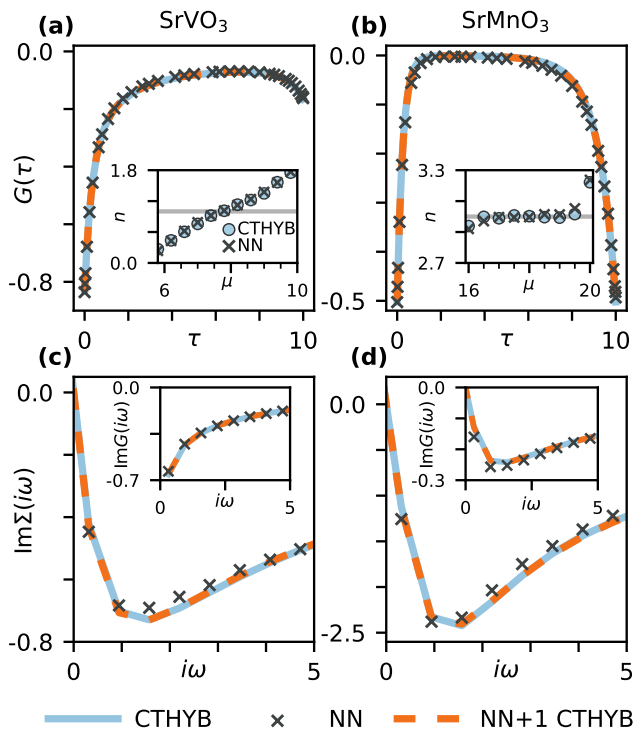


FIG. 3. DFT+DMFT results for SrVO₃ (left) and SrMnO₃ (right) at $\beta = 10$ using GNet (crosses) for $M = 3$ orbitals at $\beta = 10$, CTHYB (solid blue), and a converged computation with the GNet solver followed by one iteration with CTHYB (NN+1×CTHYB, dashed red). For each material, we show $G(\tau)$ (top), $\text{Im}\Sigma(i\omega)$ (bottom), and $\text{Im}G(i\omega)$ (bottom, insets). Top insets: impurity occupancy $n(\mu)$ with the NN density-solver (crosses) and CTHYB (circles).

hybridization functions without information on material specifications.

Neural network QI solvers run very quickly (typically within one second), but they lack any accuracy guarantee or error bars and, as seen for example in the lower panels of Figure 3 the results are not exactly identical to the numerically exact results. This issue motivates a *NN-accelerated strategy* [17, 21]: use the NN solver to rapidly obtain a converged solution, then refine and validate with a few iterations of an exact but expensive solver. Figure 3 (dashed red line) demonstrates this approach—a single CTHYB iteration initialized from the GNet solution yields self-energies in excellent agreement with the full reference calculation (differences in G and Σ are shown in Appendix E). Figure 4 further illustrates the acceleration, comparing the DMFT convergence for three physical quantities—impurity occupancy n_{imp} , self-energy Σ , and Green’s function G —using two different initializations. The NN-initialized calculation (crosses, red) converges substantially faster than the conventional DMFT calculation (circles, blue), which starts from a DFT calculation and updates the chemical potential given the target density n_{latt} from the DFT.

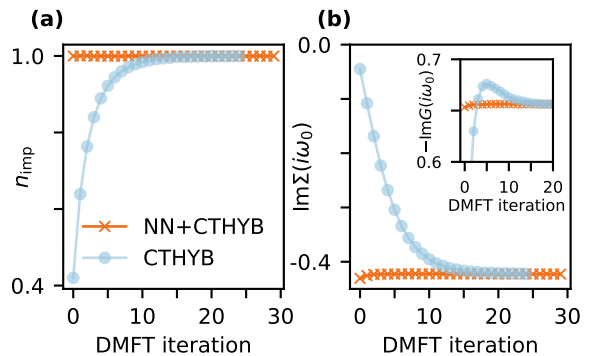


FIG. 4. Convergence of the impurity occupancy n_{imp} (a), $\text{Im}\Sigma(i\omega_0)$ (b), $\text{Im}G(i\omega_0)$ (inset), vs the iterations of the DMFT self-consistency loop, using CTHYB, starting from a DFT solution (circle, blue) and updating μ or a converged DMFT computation using GNet and density solvers (cross, red), for the case of SrVO₃. Here, $i\omega_0$ denotes the first Matsubara frequency.

Since obtaining the initial NN solution adds negligible cost compared to exact solver iterations, this strategy achieves an overall speedup of approximately one order of magnitude in this example.

Discussion— In this paper, we have presented neural-network-based solvers for an important class of quantum many-body systems: the quantum impurity models central to quantum embedding approaches for the electronic structure of materials with strong electronic correlations. We have quantified their accuracy by benchmarking them against numerically exact quantum Monte Carlo results.

By constructing our training dataset independently of materials-specific details — except for the form of the atomic interaction and the number of orbitals — we obtain a generic quantum impurity solver directly applicable to any DMFT computation within its specified parameter range. The success of our solver in DFT+DMFT computations of SrVO₃ and SrMnO₃ indicates that our synthetic dataset is sufficiently rich to cover the relevant hybridization function space encountered in realistic materials calculations.

When used free-standing, the NN solvers achieve speedups of several orders of magnitude (seconds versus hours or days) compared to existing techniques while maintaining good accuracy. When used to initialize a conventional calculation, they achieve acceleration by 1-2 orders of magnitude (1-2 iterations versus 10-30) with very high accuracy. This neural-network-based acceleration has transformative potential for DFT+DMFT electronic structure calculations.

Future applications may include fast computation of total energies, forces, structural relaxation, phonon spectra, large supercells with correlated atoms, and parameter space searches for materials design. Various generalizations of neural network solvers should also be explored. An important open question in this context is the generation of synthetic data sets with appropriate coverage of

the needed function space. Near term research targets include extending the NN solvers to include spin-orbit coupling, more orbitals, and the spatial correlations incorporated in cluster dynamical mean field theory. Also interesting are extensions to higher-order correlation functions such as response or vertex functions, real-time dynamics, and retarded interactions as in GW+DMFT.

Acknowledgements — The work of AJM at Columbia University was supported by Programmable Quantum Materials, an Energy Frontier Research Center funded

by the U.S. Department of Energy (DOE), Office of Science, Basic Energy Sciences (BES), under award DESC0019443. We are grateful to Michel Ferrero, Rudy Morel, and Filippo Vicentini for useful discussions. IP and AV thank Harry LaBollita for technical support. The Flatiron Institute is a division of the Simons Foundation.

Data availability — Data and code are available upon reasonable request to the authors. A trained model for one orbital and an example calculation are publicly available [32].

-
- [1] P. A. M. Dirac, *Proceedings of the Royal Society of London. Series A, Containing Papers of a Mathematical and Physical Character* **123**, 714 (1929).
- [2] A. Georges and G. Kotliar, *Phys. Rev. B* **45**, 6479 (1992).
- [3] A. Georges, G. Kotliar, W. Krauth, and M. J. Rozenberg, *Rev. Mod. Phys.* **68**, 13 (1996).
- [4] G. Kotliar, S. Y. Savrasov, K. Haule, V. S. Oudovenko, O. Parcollet, and C. Marianetti, *Rev. Mod. Phys.* **78**, 865 (2006).
- [5] E. Gull, A. J. Millis, A. I. Lichtenstein, A. N. Rubtsov, M. Troyer, and P. Werner, *Rev. Mod. Phys.* **83**, 349 (2011).
- [6] P. Werner, A. Comanac, L. De’Medici, M. Troyer, and A. J. Millis, *Phys. Rev. Lett.* **97**, 076405 (2006).
- [7] P. Werner and A. J. Millis, *Phys. Rev. B—Condensed Matter and Materials Physics* **74**, 155107 (2006).
- [8] A. N. Rubtsov, V. V. Savkin, and A. I. Lichtenstein, *Phys. Rev. B—Condensed Matter and Materials Physics* **72**, 035122 (2005).
- [9] E. Gull, P. Werner, O. Parcollet, and M. Troyer, *Europhys. Lett.* **82**, 57003 (2008).
- [10] R. Bulla, T. A. Costi, and T. Pruschke, *Rev. Mod. Phys.* **80**, 395 (2008).
- [11] R. Bulla, *Phys. Rev. Lett.* **83**, 136 (1999).
- [12] S. R. White, *Phys. Rev. Lett.* **69**, 2863 (1992).
- [13] U. Schollwöck, *Rev. Mod. Phys.* **77**, 259 (2005).
- [14] S. Östlund and S. Rommer, *Phys. Rev. Lett.* **75**, 3537 (1995).
- [15] V. Anisimov, A. Poteryaev, M. Korotin, A. Anokhin, and G. Kotliar, *J. Phys. Condens. Matter.* **9**, 7359 (1997).
- [16] A. I. Lichtenstein and M. I. Katsnelson, *Phys. Rev. B* **57**, 6884 (1998).
- [17] L.-F. Arsenault, A. Lopez-Bezanilla, O. A. Von Lilienfeld, and A. J. Millis, *Phys. Rev. B* **90**, 155136 (2014).
- [18] E. Sheridan, C. Rhodes, F. Jamet, I. Rungger, and C. Weber, *Phys. Rev. B* **104**, 205120 (2021).
- [19] E. J. Sturm, M. R. Carbone, D. Lu, A. Weichselbaum, and R. M. Konik, *Phys. Rev. B* **103**, 245118 (2021).
- [20] E. Agapov, O. Bertomeu, A. Carballo, C. B. Mendl, and A. Sander, arXiv:2411.13644 (2024).
- [21] H. Lee, Z. Zhao, G. H. Booth, W. Ge, and C. Weber, *Phys. Rev. B* **112**, 035165 (2025).
- [22] P. Mitra and H. Banerjee, *chemrxiv-2025-dp7rd* (2025).
- [23] R. Rao and L. Zhu, arXiv:2512.25061 (2026).
- [24] J. Kaye, K. Chen, and O. Parcollet, *Phys. Rev. B* **105**, 235115 (2022).
- [25] Alternatively, this can be seen as the exact solution of a fully-connected Hubbard model with random hopping, in which case no magnetic phase is present[3].
- [26] J. Kanamori, *Prog. Theor. Phys.* **30**, 275 (1963).
- [27] A. Georges, L. d. Medici, and J. Mravlje, *Annu. Rev. Condens. Matter Phys.* **4**, 137 (2013).
- [28] P. Werner and A. J. Millis, *Phys. Rev. Lett.* **99**, 126405 (2007).
- [29] A. Fujimori, I. Hase, H. Namatame, Y. Fujishima, Y. Tokura, H. Eisaki, S. Uchida, K. Takegahara, and F. De Groot, *Phys. Rev. Lett.* **69**, 1796 (1992).
- [30] K. Lee and E. Iguchi, *J. Solid State Chem.* **114**, 242 (1995).
- [31] D. Kim, H. Lee, B. Dabrowski, S. Kolesnik, J. Lee, B. Kim, B. Min, and J.-S. Kang, *Phys. Rev. B Condens. Matter* **81**, 073101 (2010).
- [32] A. Valenti and I. Park, Trained model, [LINK](#) (2026).

Appendix A: Interaction Hamiltonians

We consider the quantum impurity action given by

$$S = - \iint_0^\beta d\tau d\tau' \sum_{mm'} \sum_{\sigma} d_{m\sigma}^\dagger(\tau) \left[(\partial_\tau - \epsilon_d)_{mm'} \delta(\tau - \tau') - \Delta_{mm'}(\tau - \tau') \right] d_{m'\sigma}(\tau') + \int_0^\beta d\tau H_{\text{int}}[d^\dagger(\tau), d(\tau)] \quad (\text{A1})$$

where m, m' labels orbital and σ labels spin index. H_{int} is the local interaction Hamiltonian of the Hubbard form for one orbital and Hubbard-Kanamori form with parameters U, J for two and three orbitals. Here we restrict the formulation to a spin-diagonal and spin-independent (i.e. paramagnetic phase) hybridization function.

For one-orbital systems, we use the Hubbard interaction Hamiltonian:

$$H_{\text{int}} = U n_\uparrow n_\downarrow, \quad (\text{A2})$$

where U is the on-site Coulomb interaction.

For multi-orbital systems, we use the Hubbard-Kanamori interaction Hamiltonian:

$$\begin{aligned} H_{\text{H-K}} = & U \sum_m n_{m\uparrow} n_{m\downarrow} + U' \sum_{m \neq m'} n_{m\uparrow} n_{m'\downarrow} \\ & + (U' - J) \sum_{m < m', \sigma = \uparrow, \downarrow} n_{m\sigma} n_{m'\sigma} \\ & - J \sum_{m \neq m'} d_{m\uparrow}^\dagger d_{m\downarrow} d_{m'\downarrow}^\dagger d_{m'\uparrow} \\ & + J \sum_{m \neq m'} d_{m\uparrow}^\dagger d_{m\downarrow}^\dagger d_{m'\downarrow} d_{m'\uparrow}, \end{aligned} \quad (\text{A3})$$

where U is the intra-orbital Coulomb interaction, U' the inter-orbital interaction, and J the Hund's coupling. The last two terms of the interaction Hamiltonian corresponds to the spin-flip and pair-hopping term, both with strength J , and $U' = U - 2J$ is set from the rotational invariance of the local interaction. m and m' are the orbital indices and σ is the spin index. This Hubbard-Kanamori interaction Hamiltonian is used in both cases of 2-orbital and 3-orbital in our study.

Appendix B: Neural-network details

In this section, we explain general details on the creation of the training set and the properties of the NN solvers presented in this work. First, we define the mappings represented by the respective NN solvers.

- GNet 1-orbital:
 $f_{G1} : (\{\Delta(\tau_i)\}, U, \mu_{\text{NN}}, \beta) \rightarrow \{G(\tau_i)\},$
- GNet 2-orbital:
 $f_{G2} : (\{\Delta_{mm}(\tau_i)\}, U, \mu_{\text{NN}}, J, \Delta_{\text{cf}}) \rightarrow \{G_{mm}(\tau_i)\},$

- GNet 3-orbital:
 $f_{G3} : (\{\Delta_{mm'}(\tau_i)\}, U, \mu_{\text{NN}}, J) \rightarrow \{G_{mm'}(\tau_i)\},$
- n -solver 3-orbital:
 $f_n : (\{\Delta_{mm'}(\tau_i)\}, U, \mu_{\text{NN}}, J) \rightarrow n_m$

Here, we set $\Delta \equiv \Delta_\uparrow = \Delta_\downarrow$, i.e. assume symmetry with respect to spin flavors. In addition, we define the effective chemical potential $\mu_{\text{NN}} \equiv -(\epsilon_d - \mu)$, which the neural network takes as input (instead of separate values of ϵ_d and μ). We note that instead of directly inputting μ_{NN} into the neural network, we input the ratio μ_{NN}/U .

1. Training dataset

The general challenge in creating a training dataset consists in creating a physically meaningful dataset that contains sufficiently distinct hybridization functions, while at the same time not imposing any information about the material specifics or the converged solution of a model a-priori. We address this challenge in the following way. Training examples of the hybridization function Δ are created in separate procedures. First, we make use of the DLR representation (see Section C)

$$\Delta_{mm'}(\tau) \approx \Delta_{mm'}^{\text{DLR}}(\tau) = \sum_{k=1}^r w_{mm'}^k e^{-\omega_k \tau}. \quad (\text{B1})$$

Hybridization functions can now be generated by random choice of the DLR coefficients $w_{mm'}^k$. To ensure that the so-obtained Δ is physical, it is sufficient to ensure the constraints (i) $w^k \geq 0$ and (ii) $w_{mm'}^k = w_{m'm}^k$. In addition, the training set should balance insulating and metallic solutions. We found that such a balance can be obtained using an exponential envelope to the DLR coefficients, i.e. we choose the coefficients randomly as follows

$$w_{mm'}^k = ((1 - \epsilon)\delta_{mm'} + \epsilon) \sqrt{v_m^k v_{m'}^k}, \quad (\text{B2})$$

$$v_m^k = e^{-k\alpha_m} u_{1,m}^k u_{2,m}^k, \quad (\text{B3})$$

where $\delta_{mm'}$ is the Kronecker delta. Here, the magnitude of α_m (and $u_{1,m}^k$) influences if the solution is metallic or insulating. The parameter ϵ controls the amount of off-diagonal contributions to the hybridization function. Here, $\epsilon, \alpha_m, u_{1,m}^k, u_{2,m}^k$ are random non-negative numbers chosen in intervals that we specify in Table I, depending on the number of orbitals.

In the first step of creating the dataset, we generate a set of hybridization functions by the procedure detailed above. We solve the impurity problems defined by these hybridization functions and randomly chosen parameters U, μ_{NN} (intervals specified below), with the help of CTSEG or CTHYB, and arrive at a set \mathcal{D}_∞ of input-label pairs. The inputs are $\mathcal{D}_{1,\text{inputs}} = (\{\Delta_{mm'}(\tau_i)\}, U, \mu_{\text{NN}}, \dots)$ (we do not explicitly write out all input parameters as they depend on the number of

Impurity model parameters						Parameters for generating Δ				
n_{orb}	β	U	μ_{NN}	J	Δ_{cf}	ϵ	α_m	$u_{1,m}^k$	$u_{2,m}^k$	N_{train}
1	[10, 80]	[0, 7]	[0, U]	–	–	0	[0, 0.3]	[0, 1]	[0, 1]	16028
2	50	[0, 10]	$\frac{3}{2}U - \frac{5}{2}J$	[0, 0.3 U]	[0, 3.5]	0	[0, 0.35]	[0, 1]	[0, 1]	18182
3	10	[0, 7]	$[-U, 4U]$	[0, 0.28 U]	–	0.1	[0, 0.35]	[0, 1]	[0, 1]	86431

TABLE I. Summary of the parameters used to create training datasets for GNet, where the total number of training examples is denoted by N_{train} . The n -solver utilizes the same dataset as the 3-orbital GNet. We note that for both the 1-orbital as well as the 3-orbital case, extra data is created at half-filling to facilitate the network’s task to learn symmetries. In the 3-orbital case, the DLR coefficients are multiplied by an overall scale of 0.2. QMC simulations were performed using 100000 CTSEG cycles in the 1-orbital case, 400000 CTHYB cycles in the 2-orbital case and 300000 CTHYB cycles for 3 orbitals.

orbitals considered) and the labels are the corresponding Green’s function solutions $\mathcal{D}_{1,\text{labels}} := \{G_{mm'}(\tau_i)\}$. The labels are obtained via CTSEG or CTHYB on the input parameters. In the special case of the n -solver, the labels are the densities n_m .

However, obtaining a well-balanced training data set solely by tuning the parameters in Eq. B3 is in general a daunting task, and requires by-hand fine-tuning. We have found that we can balance the training set in a straightforward way by adding a second step to the training data generation. In particular, we construct a set \mathcal{D}_2 that we use to enhance our training dataset. It consists of n_2 inputs of the form $(\{\Delta_{mm'}(\tau_i)\}, U, \mu_{\text{NN}}, \dots)$, where we choose $\{\Delta_{mm'}(\tau_i)\} \in \mathcal{D}_{1,\text{labels}}$. If $U, \mu_{\text{NN}}, \dots$ have the same values as chosen for the set $\mathcal{D}_{1,\text{inputs}}$, this would correspond to the second DMFT-iteration on the Bethe lattice ($\Delta = G$ self-consistency condition). Here, we include both a set with $U, \mu_{\text{NN}}, \dots$ to have the same values as in $\mathcal{D}_{1,\text{inputs}}$, as well as new random choices for these parameters. This procedure has the goal to construct a meaningful “randomness” for hybridization functions. Then, CTSEG or CTHYB on these inputs creates the corresponding labels. This procedure can in principle be iterated with new random values of $U, \mu_{\text{NN}}, \dots$ to create distinct, physically meaningful hybridization functions, that at the same time do *not* correspond to specific DMFT solutions and are thus agnostic to the model application. We repeat the procedure 1–2 times. The total training set is the combination of all of the so-obtained data. Table I summarizes the intervals chosen for the involved random parameters for each solver, the size of the training set and the computational cost to generate it.

The ranges of U, μ_{NN} and J are chosen to span physically relevant parameter regimes. The range of μ_{NN} , in particular, is chosen to ensure that the training dataset should cover the whole range of electron occupancies $N = 0 - 2m$ (with exception of the 2-orbital case, where we trained on half-filling only). The neural network takes the effective chemical potential μ_{NN} as an input, which is randomly sampled as a ratio of U ,

$$\mu_{\text{NN}}/U \in [0, \alpha]. \quad (\text{B4})$$

In a simple one-orbital atomic limit, the energies of the $N = 1$ and $N = 2$ states are given by $E(N = 1) = \epsilon_d - \mu$ and $E(N = 2) = \epsilon_d - \mu + U$, respectively, therefore

$\alpha = 1$ can cover all possible occupancies $N = 0, 1, 2$ (see Table I). From this relation, half-filling corresponds to $\mu_{\text{eff}} = U/2$.

For general multi-orbital systems relevant to real materials, the relation between μ and the electron occupancy n becomes nontrivial, not only because of the multi-orbital Coulomb interaction terms in the Hamiltonian but also the dispersion of the density of states. Nevertheless, the dominant scale controlling charge filling can be set by the “Hartree” (mean-field) energy with some additional padding for the effect of bandwidth. In the case of t_{2g} -orbitals with Kanamori interaction, for example, the Hartree energy, the mean-field energy taking account of only density-density terms, can be written as:

$$E_{\text{Hartree}} = U \langle n_{m\sigma} \rangle + (U' - J) \sum_{m'} \langle n_{m'\sigma} \rangle + U' \sum_{m'} \langle n_{m'\bar{\sigma}} \rangle. \quad (\text{B5})$$

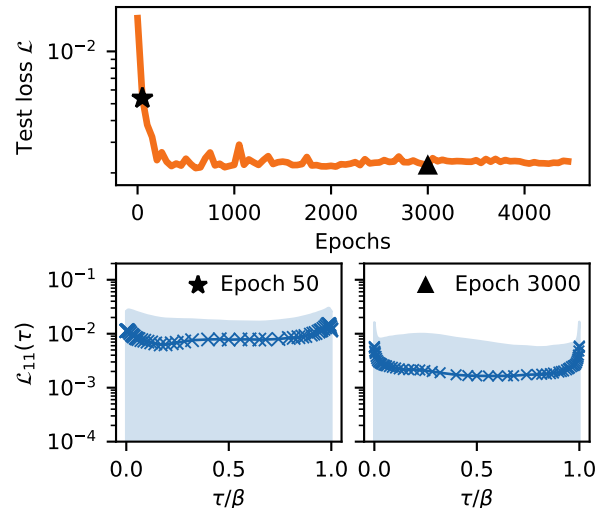


FIG. 5. Upper panel: Test loss of the 1-orbital NN solver as a function of number of epochs. Lower panels: Averaged distance as defined in Eq. (B9), for epochs 50 (left) and 3000 (right). The line and crosses are this averaged distance, the blue shaded regions indicate the standard deviation of this measure over the test set.

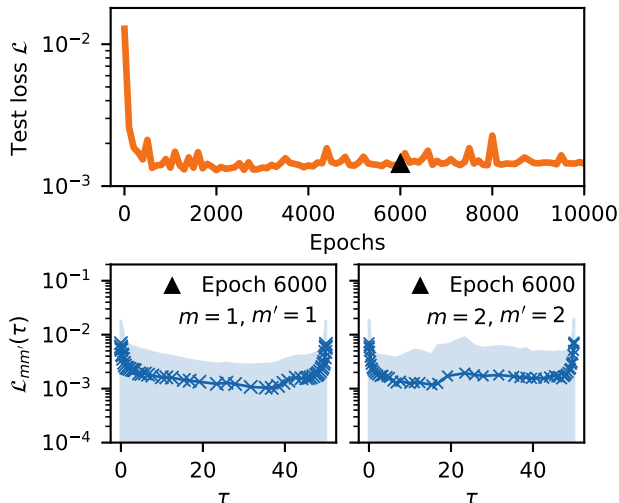


FIG. 6. Upper panel: Test loss of the 2-orbital $GNet$ as a function of number of epochs. Lower panels: Averaged distance as defined in Eq. (B9), for the epoch 6000. On the RHS, the averaged distance is plotted for orbital 1, on the LHS, for orbital 2. The line and crosses are this averaged distance, the blue shaded regions indicate the standard deviation of this measure over the test set.

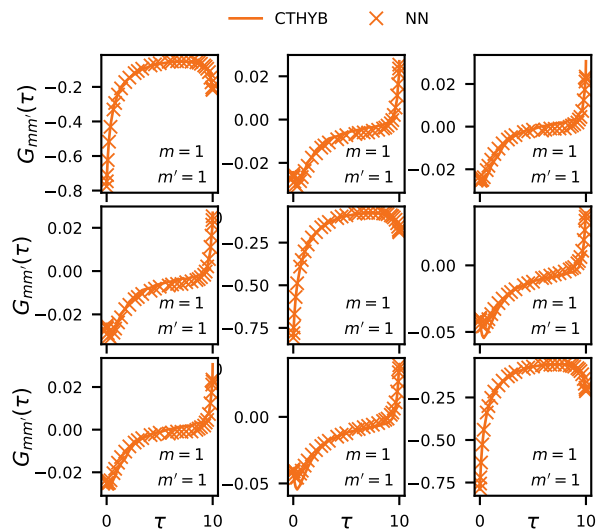


FIG. 7. Example (single-shot) impurity solution for $U \approx 6.56$, $\mu \approx 0.59$, $J = 0.83$, with $GNet$ and CTHYB given the same input Δ (with non-zero offdiagonal components), for the 3-orbital case.

In the $M = 3$ case, reaching the fully occupied state $N = 6$ requires the interaction energy, which yields an upper bound

$$\mu_{\text{eff}, N=6} = 5(U - 2J), \quad (\text{B6})$$

which corresponds to the additional interaction energy to

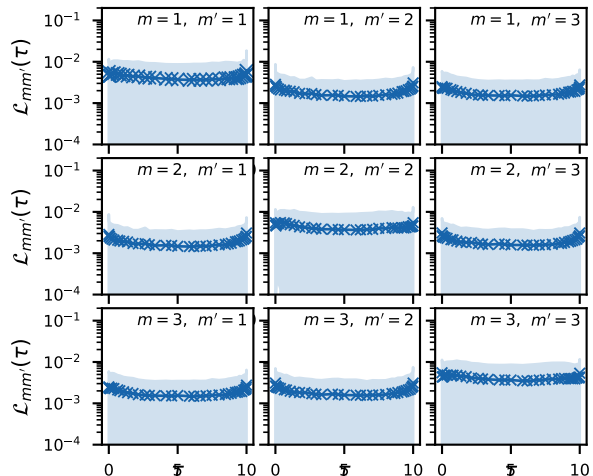


FIG. 8. Averaged distance as defined in Eq. (B9), after training (for the epoch 10000) in the 3-orbital case.

add an electron to $N = 5$ state.

In realistic systems, this range of μ can be further broadened by a finite bandwidth W . Taking this into account, and noting that we sample $J \in [0, 0.28)U$, choosing $\alpha \approx 5$ provides a reasonable coverage of all relevant occupancies from empty to fully-filled states, for the $M = 3$ case. In practice, to train the solver for strong correlation phenomena which occurs far away from empty or fully-filled states, we can narrow the sampled μ range down. Thus, our choice of $\mu_{\text{NN}} \in [-U, 4U)$ safely spans the physically relevant filling range with strong correlation effects.

2. Architecture

GNet 1-orbital. We use a Multilayer Perceptron (MLP) with 4 layers and geLU activation function. The input $(\{\Delta(\tau_i)\}, U, \mu_{\text{NN}}, \beta)$ is flattened into a vector. Crucially, the parameters U, μ, β are in addition embedded using two smaller hidden layers, and the output of these hidden layers is fed into each hidden layer of the main network. This procedure emphasizes the relevance of the parameters U, μ, β and the distinction to the hybridization function. The total number of optimizable parameters is 560289.

GNet 2-orbital. The architecture follows the same principle as in the 1-orbital case, but with 5 instead of 4 layers, and skip connections. $(\{\Delta_{mm'}(\tau_i)\}, U, \mu_{\text{NN}}, J, \Delta_{\text{cf}})$ is flattened into a vector and the parameters $U, \mu_{\text{NN}}, J, \Delta_{\text{cf}}$ are in addition embedded using 2–3 smaller hidden layers. The output of this embedding is fed into each hidden layer of the main network. The total number of optimizable parameters is

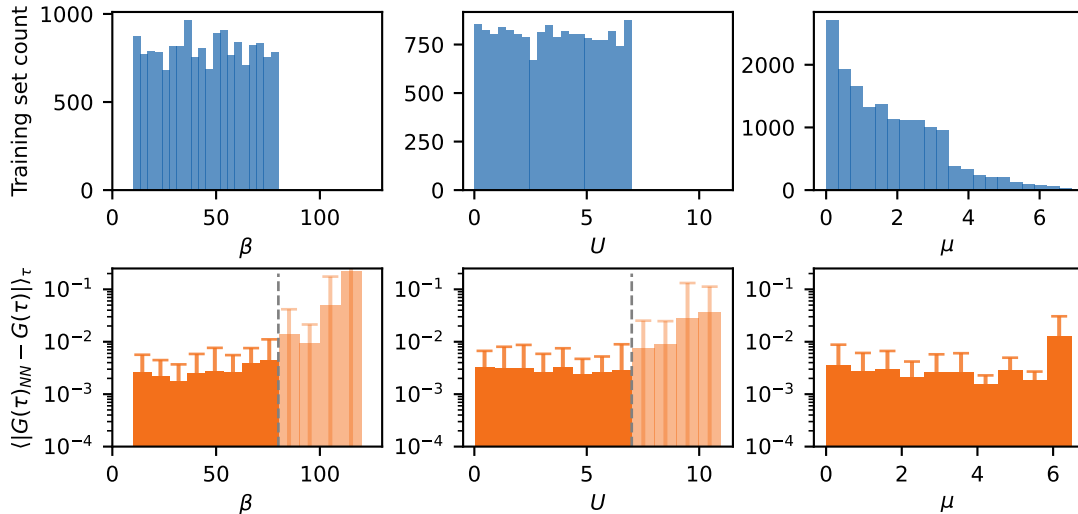


FIG. 9. Upper panels: Distribution of training examples for the 1-orbital NN solver over the parameters β , U , μ . Lower panels: Averaged distance $\sum_{\tau} |G_{NN}(\tau) - G(\tau)|$, for epoch 3000, distributed over parameter values taken from a separate test set. The average is taken over all τ values. The dashed grey line indicates the parameter boundaries of the training set. We note that the test set utilized for the lower panel is distinct from the “standard” test set utilized in Fig. 5, since it includes parameter values of β and U outside the trained range.

2451834.

GNet 3-orbital. We utilize a residual neural network (ResNet), in order to account for both trainability and increased model size in comparison to the 1-and 2-orbital case (the number of optimizable parameters is 17676720). The input consists of a flattened vector of the quantities $(\{\Delta_{mm'}(\tau_i)\}, U, \mu_{NN}, J) \rightarrow \{G_{mm'}(\tau_i)\}$. We note that we did not see improvement in additionally feeding U, μ_{NN}, J into each layer, as in the case for the 1-and 2-orbital solver.

n-solver 3-orbital. The n -solver is constructed by fine-tuning the *GNet 3-orbital* model. In particular, we add 3 additional hidden layers to the *GNet* architecture, with the final output layer of size 3 (each output neuron corresponding to the density n_m in orbital m). These 3 additional hidden layers contain 125411 parameters in total. The model is trained by loading the final *GNet* checkpoint and continuing training with the additional layers.

3. Training and generalization

We utilize a mean squared loss for training. In particular, in the case of the *GNet* solvers, the mean squared loss corresponds to

$$\mathcal{L} = \sum_{m \leq m'} \mathcal{L}_{mm'}, \quad (\text{B7})$$

$$\mathcal{L}_{mm'} = \frac{1}{|\mathcal{D}|} \sum_{j \in \mathcal{D}} \sum_i |G_{mm'}^{\text{NN}}(\tau_i) - G_{mm'}^{\text{label}}(\tau_i)|^2, \quad (\text{B8})$$

where G^{NN} (G^{label}) denotes the neural-network output (“ground truth” Green’s function obtained via quantum Monte Carlo). The index j runs over all input - label pairs in the set \mathcal{D} . We show the loss \mathcal{L} evaluated on a test set $\mathcal{D}_{\text{test}}$ as a function of training epochs in the upper panel of Fig. 5 for the 1-orbital case, and in the upper panel of Fig. 6 for the 2-orbital case.

In addition, we investigate whether the accuracy of the neural-network prediction depends on the value of τ . For this purpose, we plot the imaginary-time dependent mean squared loss, i.e.

$$\mathcal{L}_{mm'}(\tau_i) = \frac{1}{|\mathcal{D}|} \sum_{j \in \mathcal{D}} |G_{mm'}^{\text{NN}}(\tau_i) - G_{mm'}^{\text{label}}(\tau_i)|^2. \quad (\text{B9})$$

This quantity is plotted for $\mathcal{D} = \mathcal{D}_{\text{test}}$ in the lower panel of Fig 5, early in training (Epoch 50) and after convergence (Epoch 3000) in the 1-orbital case. We find that G is learned to higher precision at intermediate values of $\tau \approx \beta/2$, and has a comparably larger error at the edges $\tau \approx 0, \beta$ (reflecting uncertainties in the density estimation). This potentially stems from typically larger absolute values of variation of the Green’s function at $\tau = 0$ within physical examples, reflecting different densities. A similar trend is observed in the 2-orbital case (see lower panel of Fig. 6), where we plot the imaginary-time dependent mean squared loss for the two orbitals separately (i.e. $G_{mm'}$ for $m = m' = 1$ and $m = m' = 2$) – most likely enhanced by the fact that the presence of crystal field splitting in the Hamiltonian results in largely differing values at $\tau = 0$ and $\tau = \beta$.

In the 3-orbital case we allow for non-zero off-diagonal

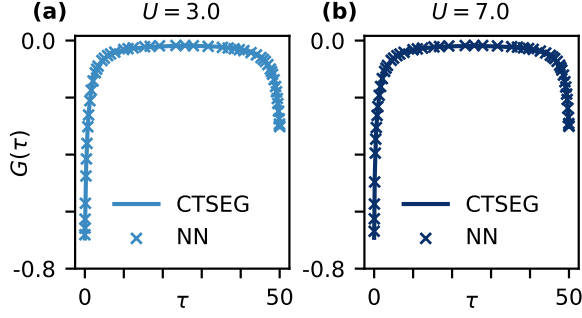


FIG. 10. GNet vs CTSEG for impurity occupancy $n = 0.6$. (a) $U = 3.0$ (b) $U = 7.0$

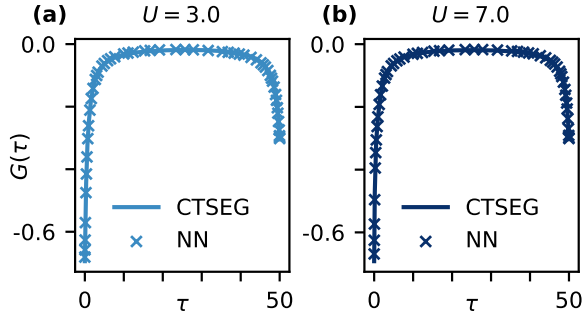


FIG. 11. GNet vs CTSEG for impurity occupancy $n = 0.8$. (a) $U = 3.0$ (b) $U = 7.0$

contributions, i.e. $m \neq m'$. We plot both an example Green's function prediction for all components of the Green's function in Fig. 7 as well as the imaginary-time dependent mean squared loss for all components in Fig. 8 after training. Here, the dependence on τ of the accuracy of the network's prediction is less enhanced than in the 1- and 2-orbital case. This may be a result of the larger expressivity of the neural-network model and the larger training set size.

We further probed the generalization abilities of the GNet 1-orbital solver for different values of β, U, μ in- and outside the range of values the network was trained on. Fig. 9 shows the result: The upper panel shows the distribution of training examples over values of β, U, μ . The lower panel shows the test loss $\mathcal{L}_{mm'}(\tau)$, plotted against values of β, U, μ in an appropriately chosen test set. Values of outside the range $[p_{min}, p_{max}]$ that the network has been trained on (with p corresponding to β or U) are colored in light color, and p_{max} marked by a grey dashed line. The error bars correspond to the standard deviation of the error in each bin. We find, that the accuracy of the network's prediction is approximately independent of β, U and μ , as long as these values are within the respective ranges the model has been trained on. The network is able to generalize outside of this range, but the error increases the further away the parameters are from the

original regime.

Appendix C: DLR representation and β transferability

In this work, we use the discrete Lehmann representation (DLR) expansion [24] to compress the imaginary time Green's function $G(\tau)$ and also take advantage of it to make neural network model β -transferable. In this section, we will briefly explain the DLR expansion for $G(\tau)$ and how we express $G(\tau)$ for different β using a single DLR mesh. In particular, we utilize a DLR mesh generated at fixed β_M , and then apply it for values of β in the range $(0, \beta_M]$.

Using the Lehmann spectral representation, the imaginary time Green's function can be written as:

$$G(\tau) = - \int_{-\infty}^{\infty} K_{\beta}(\tau, \omega) \rho(\omega) d\omega \quad \tau \in [0, \beta] \quad (\text{C1})$$

where ρ is the spectral density and K_{β} is the kernel

$$K_{\beta}(\tau, \omega) = \frac{e^{-\omega\tau}}{1 + e^{-\beta\omega}}, \quad (\text{C2})$$

in the fermionic case.

If we assume that every spectral density ρ has a finite support included in $[-\omega_{max}, \omega_{max}]$, we have

$$G(\tau) = - \frac{1}{\beta} \int_{-\Lambda}^{\Lambda} K_{\beta=1}(x, \bar{\omega}) \rho\left(\frac{\bar{\omega}}{\beta}\right) d\bar{\omega} \quad (\text{C3})$$

where $x \equiv \frac{\tau}{\beta}$ and $\Lambda = \beta\omega_{max}$. In the DLR representation, the basis only depends on Λ and the precision [24].

Equation (C3) shows that we can represent the Green's functions at various temperatures as function of $x \in [0, 1]$ (hence on the same interval), if we take a DLR basis with cut-off $\Lambda = \beta_M\omega_{max}$.

The number of DLR basis increases with β_M . However, in practice, it is sufficient to consider a logarithmically spaced range of β , e.g. $\beta \in [10, 100]$. In our study, we used the range of $\beta \in [10, 80]$, $\omega_{max} = 10$, and $\epsilon = 1\text{E} - 13$.

To cover larger ranges of temperatures, this procedure could in principle be generated to train separate solvers for various ranges of temperatures - for instance, training of a separate solver for the range $\beta \in [80, 200]$, with the DLR grid generated at $\beta = 200$.

Appendix D: 1-orbital model

1. Non-half-filled cases

Following the comparison shown in Figure 1 of the main text, GNet solver trained for $M = 1$ orbital at the range of $\beta \in [10, 80]$ is also tested for non-half-filled cases. Figures 10 (for $n = 0.6$) and 11 (for $n = 0.8$)

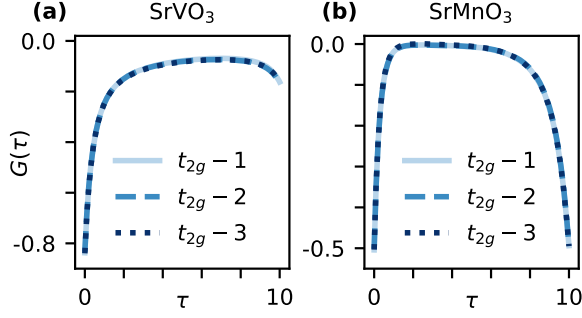


FIG. 12. NN Green's function shown for all 3 t_{2g} orbitals in the case of SrVO₃ (a) and SrMnO₃ (b).

show the comparison between *G*Net and CTSEG solvers for small ($U = 3$) and large ($U = 7$) U vales, where $n = 1$ corresponds to half-filled case. The calculations was done at $\beta = 50$, and again, the *G*Net solver shows an excellent agreement to CTSEG solver results.

Appendix E: 3-orbital Materials

The *G*Net solver does not impose any symmetry constraints in general multi-orbital problems. In other words, both the input hybridization function and the output Green's function are $M \times M$ (ignoring spin) block matrices, whose diagonal blocks can differ from

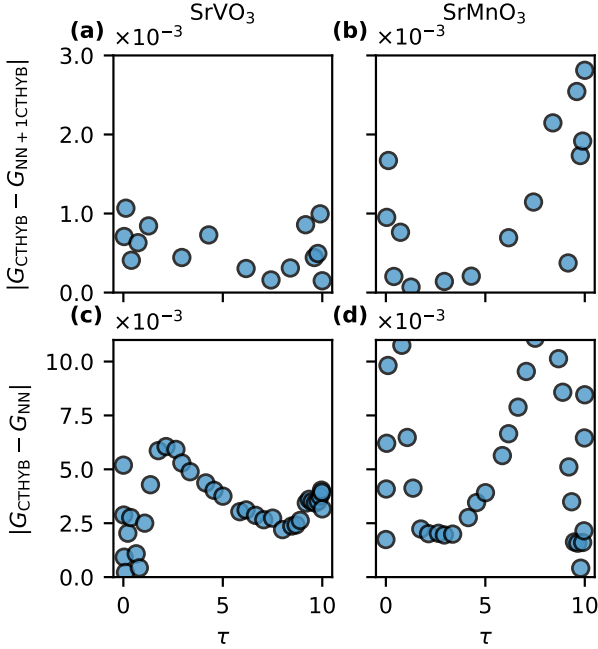


FIG. 13. Difference in $G(\tau)$. $|G_{\text{CTHYB}} - G_{\text{NN}+1\text{CTHYB}}|$ for SrVO₃ (a) and SrMnO₃ (b). $|G_{\text{CTHYB}} - G_{\text{NN}}|$ for SrVO₃ (c) and SrMnO₃ (d).

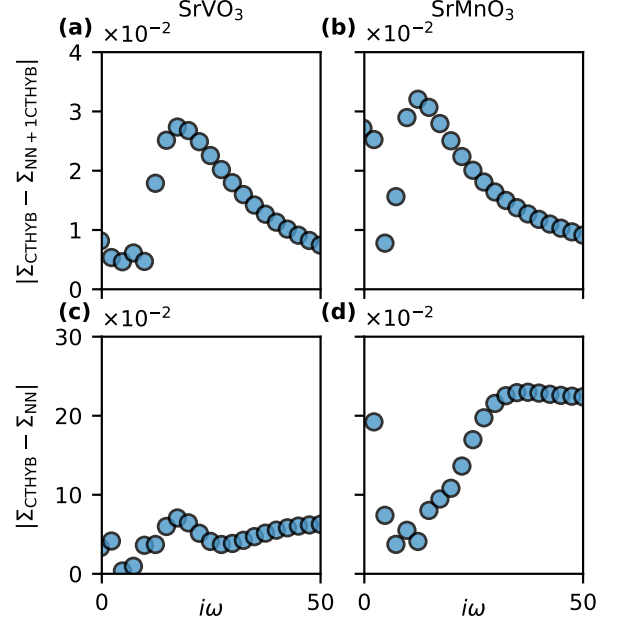


FIG. 14. Difference in $\Sigma(i\omega)$. $|\Sigma_{\text{CTHYB}} - \Sigma_{\text{NN}+1\text{CTHYB}}|$ for SrVO₃ (a) and SrMnO₃ (b). $|\Sigma_{\text{CTHYB}} - \Sigma_{\text{NN}}|$ for SrVO₃ (c) and SrMnO₃ (d).

each other and whose off-diagonal blocks can be non-vanishing. The non-degenerate two-orbital system with crystal-field splitting presented in the main text is an example of a case with different diagonal blocks. This absence of enforced symmetry is in fact a general property shared by conventional impurity solvers such as CTQMC.

It is therefore essential that the *G*Net solver be able to predict the Green's function with the symmetry expected from the symmetry of the local Hamiltonian and the interaction Hamiltonian. In other words, while the solver does not assume any symmetry a priori, it has to predict the Green's function with the physically required symmetry whenever it is present in the problem, up to numerical error.

For the real material examples considered in this work, SrVO₃ and SrMnO₃, the local octahedral ligand field enforces a threefold degeneracy of t_{2g} orbitals of an impurity problem. Consequently, the (DFT) hybridization function is block diagonal (in principle, and in practice as well) with vanishing off-block-diagonal components, and the Green's function solution obtained from self-consistent DMFT loop is also expected to preserve this symmetry. In Fig. 12, we show that the *G*Net solver correctly reproduces this expected symmetric structure of the Green's function for both SrVO₃ and SrMnO₃.

Further, we show the accuracy of the *G*Net prediction of the Green's function and the self-energy in Figs. 13 and 14. In particular, we plot the difference to reference CTHYB calculations, and compare both the NN-accelerated strategy as well as solely using *G*Net.